ISSN 1027-4510, Journal of Surface Investigation: X-ray, Synchrotron and Neutron Techniques, 2024, Vol. 18, Suppl. 1, pp. S311–S320. © Pleiades Publishing, Ltd., 2024.

Tuning Surface Charge and Defects in Zinc Oxide Crystals Via Low-Energy Electron Irradiation

U. Sharopov[a, b, *], K. Samiev[b], M. Kurbanov[c], M. Karimov[c], D. Saidov[d], F. Akbarova[e], Z. Iskandarov[f], S. Islamov[f], A. Komolov[j], and S. Pshenichnyuk[h]

[a] *Physical-Technical Institute, Uzbekistan Academy of Sciences, Tashkent, 100084 Uzbekistan*
[b] *Bukhara State University, Bukhara, 200118 Uzbekistan*
[c] *Urgench State University, Urgench, 220100 Uzbekistan*
[d] *Urgench branch of the Tashkent University of Information Technologies, Urgench, 220100 Uzbekistan*
[e] *Institute of Materials Science, Tashkent, 102226 Uzbekistan*
[f] *Tashkent State Agrarian University, Tashkent, 111218 Uzbekistan*
[j] *St. Petersburg State University, St. Petersburg, 199034 Russia*
[h] *Institute of Molecule and Crystal Physics, Russian Academy of Sciences, Ufa, 450075 Russia*
**e-mail: utkirstar@gmail.com*

Received June 15, 2024; revised August 15, 2024; accepted August 25, 2024

Abstract—This work describes research on how zinc oxide (ZnO) crystals behave when bombarded with low-energy electrons (up to 600 eV). The key finding is that the energy of the electrons strongly affects what happens on the surface of the ZnO. We have identified specific electron energies that cause negative charge to build up on the surface, remove existing charge, and create gaps where oxygen atoms used to be. It was determined that depending on the energy of electrons, it is possible to tune the surface charge, which can be used for technological purposes. This knowledge could be crucial for developing new methods of creating thin films and two-dimensional structures made from ZnO, by controlling the charge of the surface.

Keywords: charge, electron irradiation, zinc oxide, surface, temperature annealing, defect formation
DOI: 10.1134/S1027451024702227

INTRODUCTION

Surface charging phenomena under electron irradiation are pivotal in understanding the dynamic interactions between electron beams and materials, especially in the fields of materials science, nanotechnology, and electron microscopy [1]. When a material is exposed to an electron beam, the incident electrons can be absorbed, transmitted, or reflected by the material's surface, leading to the accumulation of electrical charge [2]. This process is influenced by the material's conductivity, electron affinity, and the energy of the incident electrons. Surface charging can significantly affect the physical and chemical properties of the material, leading to various applications and implications in scientific research and industrial applications.

As we all know, protons and electrons are the basis of catalysis processes [3, 4]. Depending on the energy value, electrons, interacting with molecules, can stimulate various desorption and dissociative processes [5–7]. The predominance of one process over another depends on the energy of the electron [8]. Therefore, electron energy is extremely important for revealing models and mechanisms of various processes [9]. However, the process of determining the threshold of various mechanisms is very difficult in the condensed phase, since multiple scattering leads to the formation of reaction cascades (for example, desorption, dissociation, charging, the formation of radiolysis products, recombination, etc.). The advantage of low-energy electrons is that (0–100 eV) it is possible to highlight the transition boundaries of processes, including the control of surface chemistry processes, in which a large number of secondary electrons are observed. The formation of negative and positive particles on the surface is also important, in addition to the fact that research on them is rather scarce, since these processes cover most of the expected dissociative processes, as well as the processes of synthesis of new molecules, desorption and sputtering. In real systems, everything is not so simple and to establish the contribution to the observed chemical activity, in the low-energy regime we can isolate, prioritize and carefully study these individual processes.

In our work on the study of surface states, we discovered charging of the surface of semiconductors and

dielectrics (ZnO, LiF, CuO) upon irradiation with low-energy primary electrons [10, 11]. Domestic and foreign works have shown that this phenomenon with the energy of primary electrons below 100 eV has not been studied [12].

Since the ZnO crystal is a promising material and is very actively studied due to its optical and luminescent properties [13–15], we needed interest in the phenomenon of charging the surface of ZnO crystals when irradiated with electrons with an energy of 1–1000 eV by the method of total current spectroscopy to understand the structure of electronic states and the nature of chemical bonds on the surface of zinc oxide. This phenomenon of secondary electron emission [16] from ionic crystals and the accompanying charging effect when exposed to electron radiation has been studied for many years [17], but many aspects of this multifaceted phenomenon are still not understood and require further research [18]. Based on the latter circumstance, we can say that the study of problems of charging the surface of crystals has not only scientific, but also a lot of practical significance, for example, for analytical electron probe research techniques [19, 20], electron lithography [21], and space technology [22], in many modern space technologies [23–25].

This manuscript investigates the mechanisms governing surface charge accumulation in polycrystalline and single-crystal zinc oxide (ZnO) under electron irradiation. The emphasis lies on elucidating the fundamental physical processes involved, exploring the factors that influence charging behavior, and outlining strategies to mitigate associated undesirable effects. By offering a critical analysis of recent advancements and highlighting the remaining challenges, this work aims to contribute to a deeper understanding of electron-material interactions within ZnO. This knowledge will pave the way for the development of novel methodologies to control and harness surface charge across diverse scientific and technological domains, including the potential exploitation of negative surface charge for the targeted growth of crystals and films. Previously, using total current spectroscopy [26], we studied the energy dependences of defect formation in ZnO crystals [10]. This paper presents the results of a further study of the kinetics and temperature dependences of the formation of negative charging and defects on the ZnO surface under electron irradiation. The thresholds for charge formation were determined and an attempt was made to explain the mechanisms of the ongoing physical process.

MATERIAL AND EXPERIMENTAL METHODS

For the experimental realization of total current spectroscopy in its simplest configuration, a measuring circuit as depicted in Fig. 1 is indispensable. A focused monokinetic electron beam (part 1 of Fig. 1) is directed towards the sample surface utilizing an electron-optical system (part 2 of Fig. 1). Within the region between the forming system and the planar sample (part 5 of Fig. 1), electrons traverse in a homogeneous retarding field, reaching the sample with an energy dictated by the displacement potential (U_d). The primary electron current (I_1) is established by the magnitude of the current generated between the electron gun's cathode and the sample under investigation. Upon interaction of primary electrons with the target, a fraction of them is reflected, yielding a current of secondary electrons (I_2), while the remainder penetrates the target, contributing to the overall current passing through the sample (I). Thee quilibrium of currents is expressed as follows [26]:

$$I_1 = I + I_2. \quad (1)$$

As the magnitude of the retarding field above the sample changes, the relative potentials of the electrostatic system remain constant. Consequently, the primary electron beam retains its focus, and the current I_1 remains constant in magnitude [27, 28].Taking this fact into consideration, it can be inferred that the magnitude of the secondary electron current I_2 can be assessed by measuring the current in the target circuit I:

$$I = I_1 - I_2, \quad I_1 = \text{const}. \quad (2)$$

By applying a small (0.1–0.2 V) sinusoidal voltage with a frequency of $\omega = 1000$ Hz to the cathode unit, it is possible to modulate the primary beam in energy, and using the synchrodetection system (6-part of Fig. 1) to isolate the first derivative of the current in the sample circuit. Then the expression for the current balance will be written as:

$$\frac{dI}{dE_p} = \frac{d(I_1 - I_2)}{dE_p} = -\frac{dI_2}{dE_p} = S(E_p). \quad (3)$$

Surface cleanliness was monitored using SIMS and total current spectra. To measure the temperature on the target surface, a chromel-alumel thermocouple was used in the temperature range (20–1000°C).

To obtain total current spectra, an electron beam (part 1 of Fig. 1) with an energy of 0 × 100 eV (current ~10^{-8} A, half-width of the energy distribution of the electron beam 0.3 eV) is directed onto the surface of a zinc oxide crystal.

The technique has an ion gun operating on an ionization mechanism to use surface cleaning and ion etching of samples [29]. All studies were carried out at room temperature. The working vacuum during the research was 10^{-8} Torr.

The interpretation of the spectra of the total current of zinc oxide was carried out on the basis of the energy diagram of the formation of the fine structure shown in Fig. 2. When the energy of the primary electron beam becomes high enough to excite various defects, the probability of primary electrons leaving the solid decreases, and a peak appears in the total current spectrum curve at the corresponding energy position of the defect. The primary peak in the total current

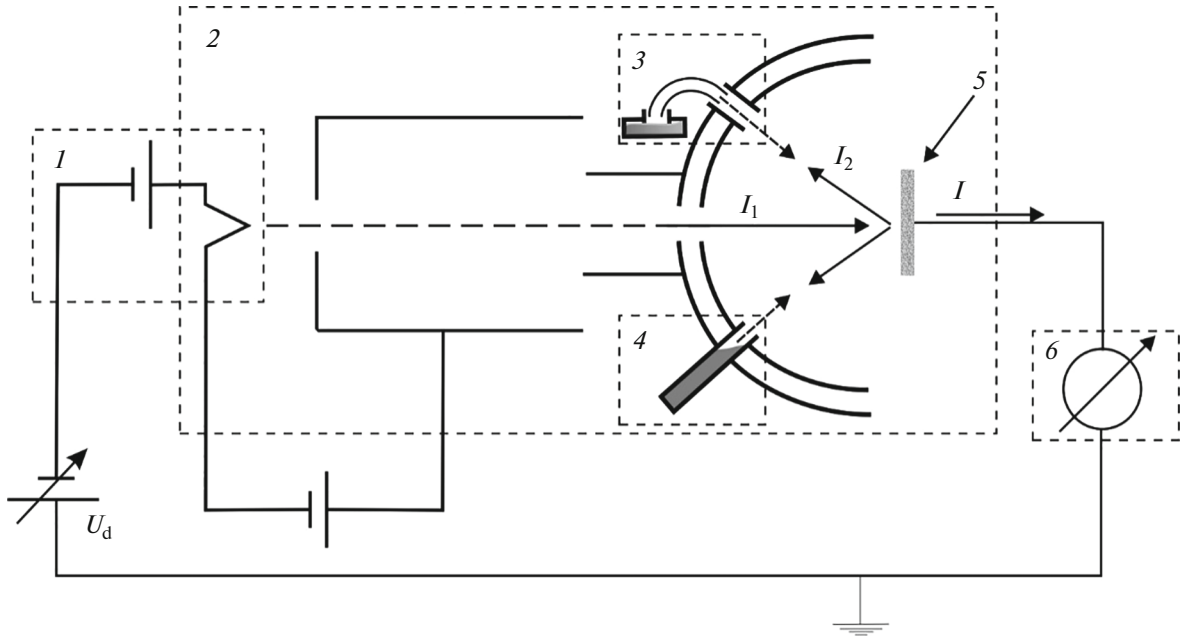

Fig. 1. Electrical circuit of the total current spectrometer, *1*—electron gun, *2*—electron-optical system, *3*—ion gun, *4*—evaporator, *5*—substrate, *6*—electronics for recording the integral current 10^{-8} A.

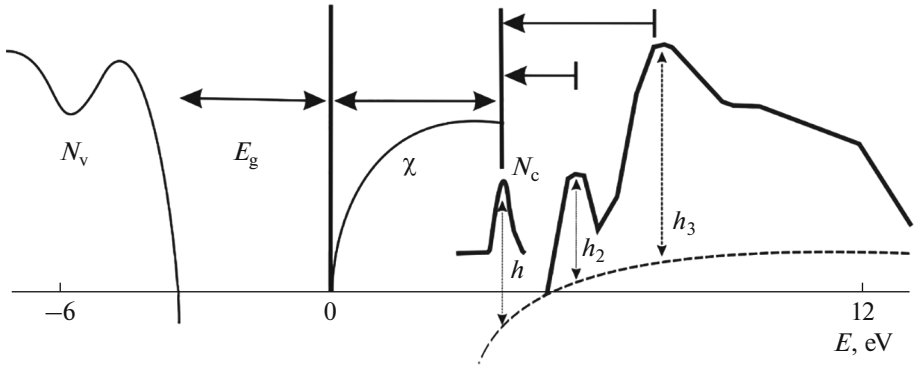

Fig. 2. Energy level diagram responsible electron transitions for the zinc oxide total current spectra fine structure.

spectra indicates the vacuum level and in all spectra the reference point is chosen (zero in Fig. 2). Also, for convenience, shifts in the total current spectra due to changes in the potential and work function of the surface are not taken into account, since the level of defects relative to the vacuum level does not change.

Each current spectrum was recorded using a fixed set of ion irradiation doses. The primary peak in all curves indicates the beginning of the counted excitation energy of defects.

In this case, the occurrence of defects, their disappearance or their transformation into other types of defects was judged by changes in the intensity (h) and half-width of the corresponding peaks (Fig. 2).

The studies were carried out in films and single crystals of ZnO, under irradiation with slow electrons, up to a certain dose ($D = 1.5 \times 10^{13}$ el/cm^2) and energy (0–600 eV). The formation of defects and their effect on the negative charging of the surface of ZnO crystals were investigated. A detailed description of total current spectroscopy methods is given in references [11, 30–32].

RESULTS AND DISCUSSION

Comparative studies were carried out and the total current spectra of poly and single ZnO crystals were obtained (Fig. 3). The first peak in the total current spectrum (peak α) is called the “primary”. It appears if the energy of the primary electron beam becomes equal to the energy position of the minimum of unoccupied electron states (DOUS—Density of Unoccu-

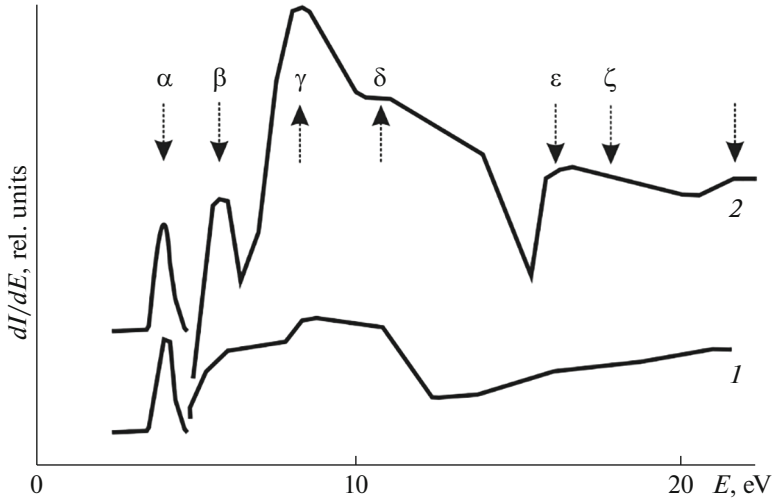

Fig. 3. Total current spectra of poly (*1*) and single crystals (*2*) of zinc oxide.

pied States), and the probability of electron penetration into the solid appears [33, 34].

As can be seen from the total current spectra, at electron energies of 4.2 eV (peak α), the excitation of interband transitions begins for both samples, which indicates the transition of electrons from the potential barrier to the conduction band, or in other words, the electrochemical potential, or also called electron affinity (for metals—work function). The difference in the total current spectra of the two samples is that the intensities of the peaks at 3.5 eV (Fig. 3, peak γ) and 8 eV (peak δ) are more weakly reflected in polycrystalline ZnO. There is also a weak formation of several peaks at excitation energies of 10, 16, 22 eV, which, according to data obtained from studies using ab initio calculations based on density functional theory (DFT), is shown in Fig. 4. As you can see, this figure more clearly represents the excitation of interband transitions from the total current spectra of zinc oxide crystals. As can be seen, the total current spectra show in more detail the band gap, electron affinity energy or surface work function (primary peak energy), unoccupied states above the Fermi level, and local states. Some peaks are consistent with the energy states of bands in the near-surface region observed in DFT calculations [35]. For example, according to DFT calculations and total current spectra, we see that the first peak (Figs. 3 and 4, peak γ) at an electron energy of 7.5 eV in the energy axis (relative to the primary peak—3.2 eV) is associated with the excitation of O2p electrons—states from the occupied valence band to unoccupied states in the conduction band, that is, the transition of an electron from the top of the valence band (VBM-valence band maximum) to the bottom of the conduction band of the zinc oxide sample (CBM-conduction band minimum). The second δ peak at 10.5 eV probably results from electron excitation of small O2p states from the lower energy of the occupied valence band to the free conduction band. The third largest peak ε at a photon energy of 16 eV (relative to the primary peak—12 eV) is attributed to the excitation electron from the 3d states of Zn from the occupied valence band to the unoccupied conduction band.

Thus, the occurrence of peaks at an energy of 3.5 eV (Fig. 3, peak γ) relative to the primary peak shows the band gap—E_g. It is also clear from the spectrum that in the band gap there is a peak at an energy of 1.8–2.0 eV (Fig. 3, peak β), which shows the presence of local states—oxygen vacancies on the surface of the sample. Also, from the spectrum we can say that on a polycrystalline sample this peak is wider (peak β—oxygen vacancies) than on a single-crystalline zinc oxide. This indicates a high concentration of surface defects of oxygen vacancies.

Analysis of the total current spectra of two crystals shows that, in a polycrystalline sample, the intensity of the peaks is very weak, due to electron scattering in the polycrystalline lattice. Also, the peak at an energy of 7.5 eV in the total current spectrum of single-crystal ZnO shows the presence of oxygen atoms at the interface with the surface, which indicates the polar orientation $(000\bar{1})$ of ZnO [36, 37].The basal planes of the crystal (0001) and $(000\bar{1})$ are polar. The (0001) plane corresponds to the surface bounded by zinc cations (Zn–ZnO), the $(000\bar{1})$ plane—by oxygen anions (O–ZnO) [38] (Fig. 5).

In previous work examining the energy dependence of zinc oxide, we showed that each resulting total current spectrum shifts toward higher energies, indicating the formation of a negative charge on the surface of the zinc oxide [10]. Figure 6 shows several spectra from previous work to explain the current data. Curve *1* shows the spectrum of the total current of zinc oxide without irradiation. Curve *2* shows the spectrum of the total current of zinc oxide after irradiation with

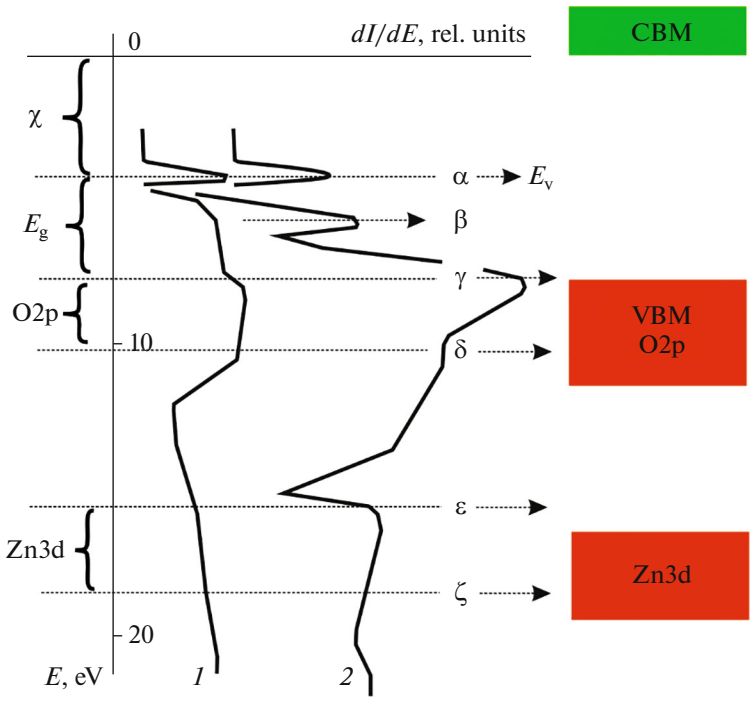

Fig. 4. Comparison of total current spectra of zinc oxide crystals with DFT calculations (*1*—polycrystal, *2*—single crystal).

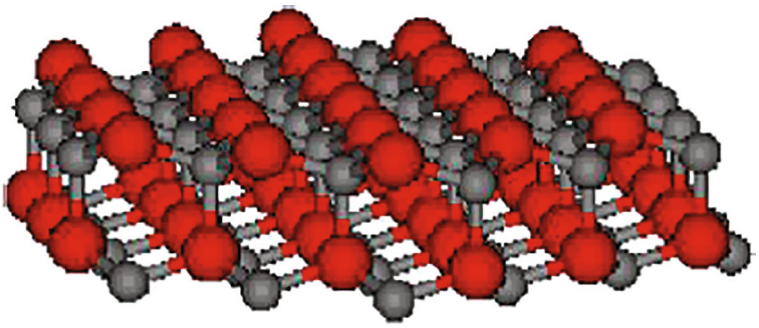

Fig. 5. Structure of the polar surface of ZnO: $(000\bar{1})$. Zinc atoms are represented by gray spheres, oxygen atoms by red spheres [39].

electrons with an energy of 10 eV. In this case (within one minute) a dose = $1.5–10^{13}$ el/cm^2 is collected on the sample. This dose was sufficient to saturate the charging on the surface, since increasing the dose did not lead to other noticeable changes on the surface of the sample. As noticeable, the spectrum has shifted to the right by about 5 eV. Further, an increase in energy by 20 eV (curve *3*) leads to a shift in the spectrum by 9–10 eV. And so on, before irradiation at energies of 115 eV, the surface potential increases to 43 eV. Further, when irradiated with electrons with an energy of 120 eV, the surface potential drops sharply to 18–20 eV and decreases to 7–8 eV at irradiation energies of 150 eV. Further, with an increase in the energy of the primary electrons, the potential of the surface of zinc oxide does not decrease or increase. The thick dashed arrow shows the direction of shift of the primary peak. This is the value of the generated potential of the surface of zinc oxide.

Figure 7 clearly shows the dependence of the change in the negative surface potential of poly and single-crystalline zinc oxide samples on the energy of electron irradiation.

As can be seen, the value of the negative charge accumulated on the surface increases to 43 eV, after the irradiation energy of the primary electrons 120 eV begins to fall, but the negative potential on the surface does not disappear and remains at the level of 7 eV.

It is also clear from the figure that the negative potential on the surface of poly and single crystal zinc oxide behaves differently. More negative potential accumulates on a polycrystalline sample than on a single-crystalline sample. This is probably due to the

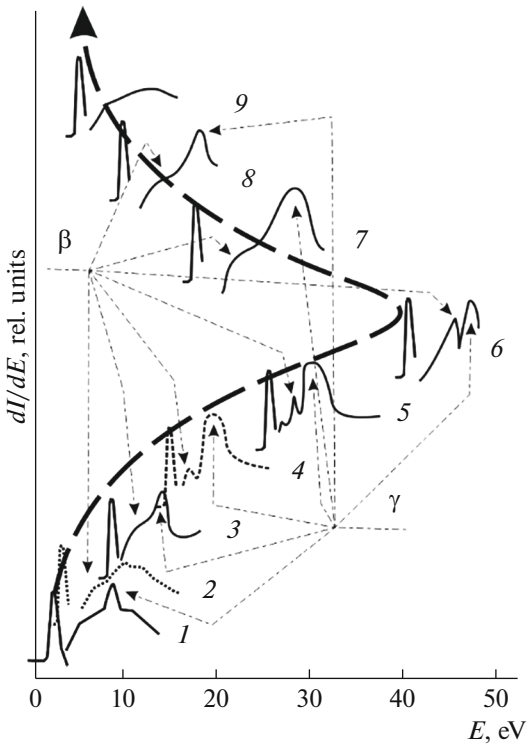

Fig. 6. Total current spectra of single-crystal zinc oxide under irradiation with slow electrons. Curves: *1*—total current spectra of the cleaned surface of zinc oxide single crystals after annealing at a temperature of 400°C; *2*—total current spectra when irradiated by electrons with energy E_{ir}—10 eV; *3*—20 eV; *4*—40 eV; *5*—50 eV; *6*—75 eV; *7*—100 eV; *8*—120 eV; *9*—130 eV; *10*—150 eV.

crystallographic orientation of atoms and their clusters on the surface or morphology. Taking morphological patterns of the surface of poly and single crystal zinc oxide can bring some clarity to the effects we observed associated with the accumulation of potential on the surface.

In previous Figs. 3, 4 and 6, we mentioned the formation of oxygen vacancies (β peak) upon electron irradiation. From the obtained total current spectra, it became clear that pre-radiation vacancies are observed on the surface of zinc oxide and their formation after irradiation with electrons. If we trace their kinetic, energy and temperature dependence, we get the following Figs. 8–10.

Figure 8 shows the energy dependence of the relative intensity of the 2.0 eV peak—an oxygen vacancy on the surface of a ZnO crystal on the energy of electron irradiation. As can be seen, before irradiation with electrons with an energy of 20 eV, the intensity of the vacancy peak does not increase significantly. This indicates the existence of pre-radiation defects on the surface of zinc oxide. With an increase in energy by 20 eV, there is a sharp jump in intensity by about 2 times, which can be attributed to the formation of vacancies due to electron irradiation. The energy region of the site can be divided into two: 1 and 2 region of electron irradiation. The first region involves vacancies that already exist (pre-radiation) on the surface of zinc oxide; here the electron energy is not enough to create vacancies.

In the second region of the irradiation section, both pre-radiation and vacancies formed during irradiation with electrons with an energy of 20 eV are involved. Further, an increase in the energy of electron irradiation does not lead to an increase in the formation of oxygen vacancies, which indicates the threshold for the formation of oxygen vacancies on the surface of the zinc oxide crystal. Thus, it is clear from the graph that an irradiation energy of 20 eV for zinc oxide is the threshold for the formation of defects on the surface; below this energy, electrons cannot create electron-hole pairs.

Figure 9 shows the temperature dependence of the relative intensity of the 2.0 eV peak—an oxygen vacancy on the surface of a ZnO crystal. As can be seen, with an increase in temperature from room temperature to 300°C, the intensity of the 2.0 eV peak does not change noticeably, which is not a characteristic behavior for vacancies. A similar situation was observed by Hoffman in his studies [40], where grown bulk ZnO crystals annealed in vacuum in zinc and oxygen vapor were characterized using optical and magnetic resonance spectroscopy. Experiments showed that the concentration of residual carriers is

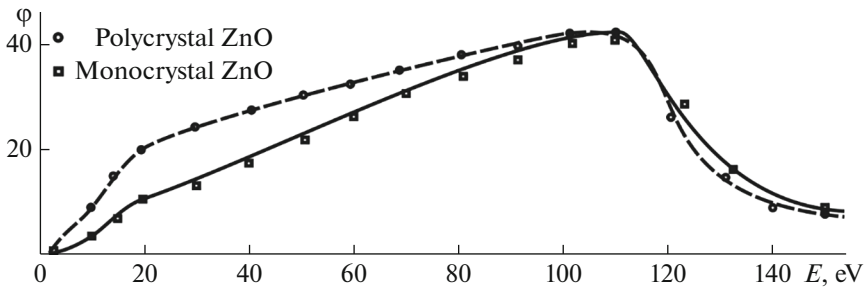

Fig. 7. Dependence of the change in the negative potential of the surface of poly and single crystal ZnO on the energy of electron irradiation.

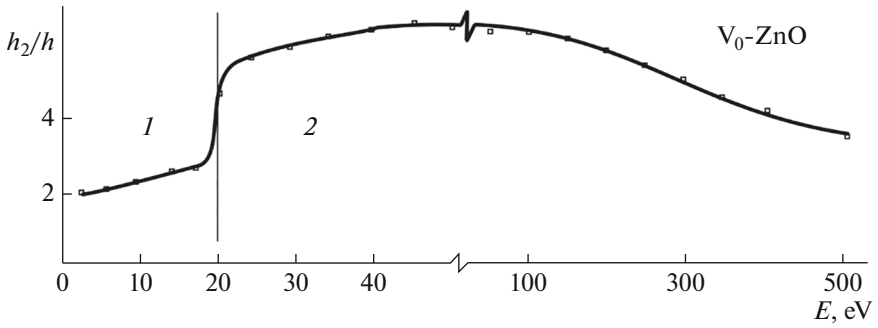

Fig. 8. Energy dependence of the relative intensity of the 2.0 eV peak—oxygen vacancy on the surface of a ZnO crystal under electron irradiation.

due to residual oxygen vacancies in the material. Annealing samples at a temperature of about 1000°C reduces the concentration of H donors and oxygen vacancies by one order of magnitude. Photoluminescence and DLTS results suggest emission at 2.45 eV (green band) and a donor level at 530 meV below the conduction band, which is associated with a doubly charged oxygen vacancy. The results indicate negative charging of oxygen vacancy defects predicted by theoretical calculations.

From the temperature dependence we can say that oxygen vacancies are not annealed up to 300°C.

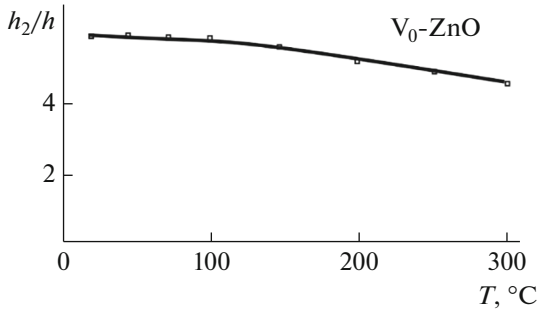

Fig. 9. Temperature T dependence of the relative intensity of the 2.0 eV peak—oxygen vacancy on the surface of a ZnO crystal.

Figure 10 shows the kinetics of the relative intensity of the 2.0 eV peak—an oxygen vacancy on the surface of a ZnO crystal. As can be seen, the intensity of the 2.0 eV peak—oxygen vacancy—drops by two times within 4 h, by five times within 8 h, and then the kinetics of vacancies does not change noticeably.

Only in this way can the concentration of oxygen vacancies on the surface be reduced, but it is impossible to completely remove vacancies from the surface.

Thus, it is clear from the graphs that the detected peak of 2.0 eV in the total current spectrum actually belongs to oxygen vacancies on the surface of the zinc oxide crystal. It reacts very stable to temperature and annealing time.

Our experiments show that in the case of electron irradiation of the ZnO surface in the energy range $1 \le E \le 20$ eV, negative charging of the surface occurs due to dissociative processes occurring below the ionization and excitation thresholds, which can only occur due to dissociative electron attachment. In this case, the formation of a negative charge due to the capture of electrons by pre-radiation oxygen vacancies. This process is considered temporary and resonant; during relaxation, the electron is simply ejected, leaving the hole in an excited state. It should be noted that the formation of charging on the surface occurs at energies below the energy of the sample band gap; this is probably due to pre-radiation vacancies.

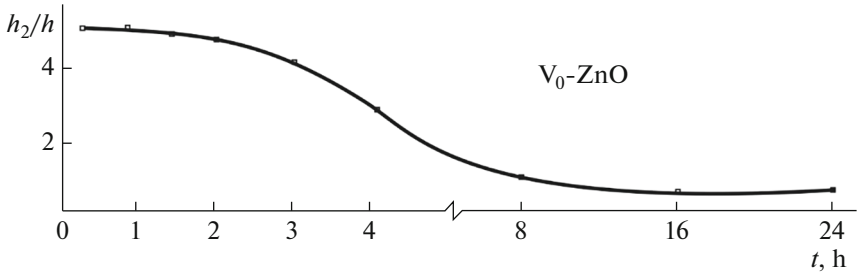

Fig. 10. Kinetics of the relative intensity of the 2.0 eV peak—oxygen vacancies on the surface of a ZnO crystal.

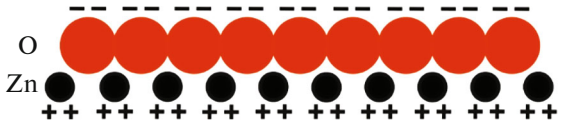

Fig. 11. Two-layer model of surface charging during electron bombardment of a semiconductor target.

The increase in the concentration of vacancies on the surface of zinc oxide at irradiation energies of 20 eV (Fig. 8) may be associated with the ionization potential of oxygen and zinc atoms. Experimentally determined [41–44], to displace an atom from a cell node from the volume, at least energy must be expended:

$$E_{disp} = 3E_{ip}, \quad (4)$$

here E_{disp} is the energy expended for displacement the atom, E_{pi} is the ionization potential of the atom (Table 1). On the surface (20.4 eV) this value is two times less than in the bulk ($13.6 \times 3 = 40.8$), since the strength of the attachment of an atom in a lattice site depends on the number of bonds, and on the surface some of them are broken. In other words, E_{pi} is less than the threshold displacement energy E_{disp}, which characterizes the formation of post-ionization defects in the volume. It seems that the electron energy is sufficient to break the bonds of the ZnO cluster into positive Zn^+ and negative O^- ions, which leads to the formation of a double-layer charge on the surface. The results show that the formed double-layer charging region on the outer side of the surface is covered with negative oxygen ions (Fig. 11).

We know that ZnO is a partially ionic crystal, and therefore its double layers consist of positively negatively charged Zn and O ions. To date, a two-layer model of surface charging under electron bombardment of a dielectric target has been developed [16, 19, 45], according to which, a layer of positive or negative charge is formed due to the emission of secondary electrons. It is also clear from our data that the ZnO $(000\bar{1})$ substrate has a surface with high reactivity (the surface is limited by oxygen ions), which, when irradiated with electrons, leads to the formation of an additional charge barrier layer, creating a potential.

Table 1. Ionization levels of zinc and oxygen (eV)

Ionization potential, eV	Zn	O
1	9.39	13.6
2	17.9	35.1
3	39.7	54.9
4	59.5	77.4
5	82.6	113.9
6	107.9	138.1
7	133.9	739.2

CONCLUSIONS

The influence of low-energy electrons ($E = 0$–600 eV) on the surface of zinc oxide crystals has been studied. In our opinion, low-energy electron irradiation of the surface of zinc oxide crystals stimulates three types of dissociative processes that occur directly as a result of inelastic collisions of electrons with surface anions and cations. These reactions cause physical and chemical processes through dissociation, breaking and formation of bonds, and atomic and molecular rearrangement of the surface of the sample. As shown, the energy of the primary electron is of paramount importance and can determine what types of primary processes can be activated on the zinc oxide surface.

In the first case, in the energy range 1 eV $\le E \le$ 20 eV, negative charging of the ZnO surface occurs due to dissociative electron attachment to pre-radiation oxygen vacancies.

In the second case, in the energy range 20 eV $\le E \le$ 120 eV, an increase in negative charging is observed due to the breaking of the bonds of the ZnO cluster into positive Zn^+ and negative O^- ions, which leads to the formation of a two-layer charge on the surface, on the outer side of the surface covered with negative oxygen ions. The energy threshold for the formation of an anion vacancy (~20 eV) on the ZnO surface was determined.

In the third case, at energies above $E \ge 120$ eV, the negative charge on the ZnO surface decreases, possibly due to oxygen ESD and other secondary electronic processes.

The data obtained from the presented work can be used to control ions and chemical reactions at the molecular level, as well as to obtain epitaxial two-dimensional thin-film heterostructures using surface potential [46]. It is safe to say that if the surface is charged during film growth, it will have a very large impact not only on the morphology of the deposited surface, but also on the structural perfection of the resulting films [47].

ACKNOWLEDGMENTS

Experiments were partly conducted according to the agreement between St. Petersburg State University and Uzbekistan National Institute for Renewable Energy Sources. Equipment of the Research Park of St. Petersburg State University, "Physical methods of surface investigation" was used within the research presented in the article.

FUNDING

This work was supported by ongoing institutional funding. No additional grants to carry out or direct this particular research were obtained.

CONFLICT OF INTEREST

The authors of this work declare that they have no conflicts of interest.

REFERENCES

1. A. Ait hssi, et al., Vacuum **217**, 112503 (2023). https://doi.org/10.1016/j.vacuum.2023.112503
2. I. Maglevanny and V. Smolar, Vacuum **46** (11), 1261 (1995). https://doi.org/10.1016/0042-207X(95)00010-0
3. A. Studer and D. P. Curran, Nat. Chem. **6** (9), 765 (2014). https://doi.org/10.1038/nchem.2031
4. A. Sytchkova, A. Belosludtsev, L. Volosevičienė, et al., Vacuum **224**, 113083 (2024). https://doi.org/10.1016/j. Vacuum.2024.113083
5. L. Sala, I. B. Szymańska, C. Dablemont, A. Lafosse, and L. Amiaud, Beilstein J. Nanotechnol. **9**, 57 (2018). https://doi.org/10.3762/bjnano.9.8
6. C. R. Arumainayagam, H.-L. Lee, R. B. Nelson, D. R. Haines, and R. P. Gunawardane, Surf. Sci. Rep. **65** (1), 1–44 (2010). https://doi.org/10.1016/j.surfrep.2009.09.001
7. E. H. H. Hasabeldaim, S. G. Menon, H. C. Swart, and R. E. Kroon, Vacuum **192**, 110447 (2021). https://doi.org/10.1016/j.vacuum.2021.110447
8. E. Böhler, J. Warneke, and P. Swiderek, Chem. Soc. Rev. **42** (24), 9219 (2013). https://doi.org/10.1039/c3cs60180c
9. S. A. Pshenichnyuk, et al., J. Chem. Phys. **155** (18), 184301 (2021). https://doi.org/10.1063/5.0072264
10. U. B. Sharopov, B. G. Atabaev, and R. Djabbarganov, J. Surf. Invest.: X-Ray, Synchrotron Neutron Tech. **14** (1), 101 (2020). https://doi.org/10.1134/S1027451020010164
11. U. B. Sharopov, K. Kulwinder, M. K.Qurbanov, et al., Thin Solid Films **735**, 138902 (2021). https://doi.org/10.1016/j.tsf.2021.138902
12. N. Cornet, et al., J. Appl. Phys. **103** (6), 064110 (2008). https://doi.org/10.1063/1.2890427
13. R. R. Jalolov, S. Z. Urolov, Z. S. Shaymardanov, S. S. Kurbanov, and B. N. Rustamova, Mater. Sci. Semicond. Process. **128**, 105783 (2021). https://doi.org/10.1016/j.mssp.2021.105783
14. S. S. Kurbanov, S. Z. Urolov, Z. S. Shaymardanov, H. D. Cho, and T. W. Kang, Semiconductors **52** (7), 897 (2018). https://doi.org/10.1134/S1063782618070126
15. I. A. Pronin, et al., Inorg. Mater. **57** (11), 1140 (2021). https://doi.org/10.1134/S0020168521110108
16. K. E. Ozerova, A. A. Tatarintsev, E. I. Rau, K. F. Minnebaev, and S. V. Zaitsev, Bull. Russ. Acad. Sci. Phys. **85**, 840 (2021). https://doi.org/10.3103/S1062873821080190
17. E. I. Rau, et al., Nucl. Instrum. Methods Phys. Res., Sect. B **266** (5), 719 (2008). https://doi.org/10.1016/J.NIMB.2007.12.093
18. E. I. Rau, A. A. Tatarintsev, E. Y. Zykova, K. E. Markovets (Ozerova), and K. F. Minnebaev, Vacuum **177**, 109373 (2020). https://doi.org/10.1016/J.VACUUM.2020.109373
19. Y. Ding, K. C. Pradel, and Z. L. J. Appl. Phys. **119** (1), 015305 (2016). https://doi.org/10.1063/1.4939618
20. A. A. Borzunov, D. V. Lukyanenko, E. I. Rau, and A. G. Yagola, J. Inverse Ill-Posed Probl. **29** (5), 753 (2021). https://doi.org/10.1515/JIIP-2020-0136/MACHINE-READABLECITATION/RIS
21. M. Bai, D. S. Pickard, C. Tanasa, M. A. McCord, C. N. Berglund, and R. F. W. Pease, *Proceedings of the 18th Bacus Symposium on Photomask Technology and Management* **3546**, 383 (1998). https://doi.org/10.1117/12.332874
22. S. S. A. An, et al., Int. J. Nanomed., (2014), p. 41. https://doi.org/10.2147/IJN.S57923
23. E. I. Rau, A. A. Tatarintsev, and E. Y. Zykova, Nucl. Instrum. Methods Phys. Res., Sect. B **460**, 141 (2019). https://doi.org/10.1016/J.NIMB.2018.12.030
24. S. K. Höeffgen, S. Metzger, and M. Steffens, Front. Phys. **8**, 318 (2020). https://doi.org/10.3389/fphy.2020.00318
25. Y. Zheng et al., Space Weather **17** (10), 1384 (2019). https://doi.org/10.1029/2018SW002042
26. S. A. Komolov and L. T. Chadderton, Surf. Sci. **90** (2), 359 (1979). https://doi.org/10.1016/0039-6028(79)90350-9
27. V. E. Henrich, Rev. Sci. Instrum. **44** (4), 456 (1973). doi 27 V. E. Henrich, Rev. Sci. Instrum., V. 44. No 4. P. 456. Apr. 1973. https://doi.org/10.1063/1.1686155
28. S. A. Pshenichnyuk, A. Modelli, N. L. Asfandiarov, E. F. Lazneva, and A. S. Komolov, J. Chem. Phys. **151** (21), 214309 (2019). https://doi.org/10.1063/1.5130152
29. U. B. Sharopov, K. Kaur, M. K. Kurbanov, D. S. Saidov, E. T. Juraev, and M. M. Sharipov, Silicon **14** (9), 4661 (2022). https://doi.org/10.1007/s12633-021-01268-0
30. R. Djabbarganov, B. G. Atabaev, Z. A. Isakhanov, and U. B. Sharopov, J. Surf. Invest.: X-Ray, Synchrotron Neutron Tech. **13** (4), 640 (2019). https://doi.org/10.1134/S1027451019040049
31. U. B. Sharopov, B. G. Atabaev, R. Djabbarganov, M. K. Kurbanov, and M. M. Sharipov, J. Surf. Invest.: X-Ray, Synchrotron Neutron Tech. **10** (1), 245 (2016). https://doi.org/10.1134/S1027451016010328
32. U. Sharopov, et al., Vacuum **213**, 112133 (2023). https://doi.org/10.1016/j.vacuum.2023.112133
33. A. S. Komolov, et al., Phys. Solid State **58** (2), 377 (2016). https://doi.org/10.1134/S106378341602013X
34. S. A. Komolov, *Total Current Spectroscopy of Surfaces* (CRC Press, 1992). https://books.google.co.uz/books/about/Total_Current_Spectroscopy_of_Surfaces.html?id=p9QQI962g4YC&redir_esc=y.
35. A. F. Wani, B. Rani, U. B. Sharopov, S. Dhiman, and K. Kaur, Int. J. Energy Res. (2022). https://doi.org/10.1002/er.7741

36. K. Mun Wong, S. M. Alay-e-Abbas, Y. Fang, A. Shaukat, and Y. Lei, J. Appl. Phys. **114** (3), 034901 (2013). https://doi.org/10.1063/1.4813517
37. P. J. Møller, S. A. Komolov, and E. F. Lazneva, A total current spectroscopy study of metal oxide surfaces: I. Unoccupied electronic states of ZnO and MgO, J. Phys.:Condens. Matter **11**, 9581 (1999). http://iopscience.iop.org/0953-8984/11/48/315
38. K. Jacobi, G. Zwicker, and A. Gutmann, Surf. Sci. **141** (1), 109 (1984). https://doi.org/10.1016/0039-6028(84)90199-7
39. C. WOLL, Prog. Surf. Sci. **82** (2–3), 55 (2007). https://doi.org/10.1016/j.progsurf.2006.12.002
40. X. Li, J. Song, Y. Liu, and H. Zeng, Curr. Appl. Phys. **14** (3), 521P (2014). https://doi.org/10.1016/j.cap.2014.01.007
41. D. R. Locker and J. M. Meese, IEEE Trans. Nucl. Sci. **19** (6), 237 (1972). https://doi.org/10.1109/TNS.1972.4326839
42. J. Meese and D. Locker, Solid State Commun. **11** (11), 1547 (1972). https://doi.org/10.1016/0038-1098(72)90517-0
43. K. Lorenz, E. Alves, E. Wendler, O. Bilani, W. Wesch, and M. Hayes, Appl. Phys. Lett. **87** (19), (2005). https://doi.org/10.1063/1.2126137
44. A. N. Dudin and V. Y. Yurina, Vestn. Amur. Gos. Univ. **97** (97), 47 (2022). https://doi.org/10.22250/20730268_2022_97_47
45. A. Melchinger and S. Hofmann, J. Appl. Phys. **78** (10), 6224 (1995). https://doi.org/10.1063/1.360569
46. J. Houplin, C. Dablemont, L. Sala, A. Lafosse, and L. Amiaud, Langmuir **31** (50), 13528 (2015). https://doi.org/10.1021/acs.langmuir.5b02109
47. M. S. Moumita Ghosh, Mater. Sci. (2023). https://doi.org/10.26434/chemrxiv-2023-v3v1x